Contents lists available at ScienceDirect

Materials & Design

Strengthening of 3D printed Cu micropillar in Cu-Ni core-shell structure

Manish Jain [a],*, Amit Sharma [a], Patrik Schürch [b], Nicolo Maria Della Ventura [a], Wabe W. Koelmans [b], Xavier Maeder [a], Jakob Schwiedrzik [a,1,*], Johann Michler [a,1]

[a] Empa Swiss Federal Laboratories for Materials Science and Engineering, Laboratory for Mechanics of Materials and Nanostructures, Feuerwerkerstrasse 39, 3602 Thun, Switzerland
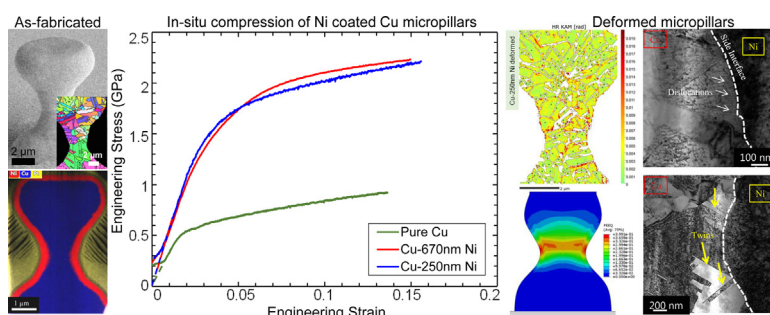[b] Exaddon AG, Sägereistrasse 25, 8152 Glattbrugg, Switzerland

HIGHLIGHTS

- Copper (Cu) micropillars were fabricated using additive micromanufacturing and subsequently coated with Nickel (Ni) to create Cu-Ni core–shell structure.
- In-situ micropillar compression revealed an exceptional $\sim$ 3-fold increase in strength after coating the Cu structure with a Ni shell.
- Experiments and FE simulation showed remarkable similarities in mechanical response and strengthening mechanism of Cu-Ni

GRAPHICAL ABSTRACT

ARTICLE INFO

ABSTRACT

Direct printing of complex 3D structures at the nano- and microscale is a promising technique for MEMS devices, small-scale sensors, and actuators. So far, most studies have been focused on printing copper (Cu) structures due to the high Coulombic efficiency compared to other conductive metals such as platinum. However, Cu suffers from low material strength, low modulus, and high strain-rate sensitivity. This work introduces a unique Cu-Ni core–shell structure for improved strength. A 3D additive-micromanufacturing technique based on localized electrodeposition was utilized to fabricate dog-bone-shaped Cu micropillars with submicron resolution. These pillars were subsequently coated with Ni by pulse-reverse electrodeposition. A combination of *in-situ* micropillar compression at various strain rates ($0.001–500 \text{ s}^{-1}$) and finite element simulations revealed remarkable strengthening in the Ni-coated Cu micropillar. Data obtained from both experiments and simulations were in good agreement, suggesting the strengthening was dominated by interface characteristics, stress redistribution, and geometrical effects. Furthermore, the study demonstrates that shape and dimension of the 3D-printed objects can be retained while increasing their strength drastically. These findings can be extended to other material systems and provide a pathway to develop strong and tough composites and metamaterials at multiple length scales for future applications.

1. Introduction

There is an ever-growing need for miniaturized components for different applications such as MEMS devices, small–scale sensors, actuators, electronic circuit elements, and ultra-high precision devices with mechanical functions [1–4]. This need resulted in a relentless drive to explore new technologies capable of creating

* Corresponding authors at: School of Mechanical and Manufacturing Engineering, University of New South Wales, 2033 Kensington, Australia (M. Jain).
E-mail addresses: manish.jain@unsw.edu.au (M. Jain), jakob.schwiedrzik@empa.ch (J. Schwiedrzik).
[1] Shared senior authorship.

three-dimensional (3D) architectures with a low defect density and sub-micrometer resolution. However, most fabrication techniques that create complex 3D nano/microstructures are subtractive. Some examples are electron beam writing [5], lithography [6,7], ultra-precision diamond machining [8] and conventional focused ion beam (FIB) milling [9,10]. These techniques often involve multiple steps of high complexity and high cost [2,11,12]. Moreover, in the case of FIB, laser ablation, and reactive ion etching [13], the fabrication process introduces damage to the sample surface that could alter the deformation behavior of the material [9,13]. Furthermore, established additive manufacturing techniques, like laser-powder bed fusion or laser/direct metal deposition, lack the resolution required for nano/micro applications due to the intrinsic size limit (10–100 μm) of the metal powder particles [14–17].

In contrast, novel additive micromanufacturing (μAM) techniques provide efficient, high resolution and flexible patterning of 3D metal microarchitectures with the smallest feature dimensions ranging from ~1 μm to ~10 μm and overall sample dimensions reaching up to several millimeters [18–21]. Direct printing of 3D nano/micro metallic architectures with controlled microstructure is useful for such applications [19]. In addition, μAM can be used to print ideal test beds - such as micropillars, micro-tensile samples, and micro-lattices suitable for mechanical testing to study process-structure–property relationships.

Several additive manufacturing techniques for micro/nano scale fabrication have recently been explored. Among the available methods, meniscus-confined electrodeposition [20], localized pulsed electrodeposition [19] and redox printing [21] are the most promising. However, the quality of the structure, e.g., surface roughness and geometry, is challenging to control. Daryadel et al. [22] reported a meniscus-confined pulsed localized electrodeposition method to fabricate nanotwinned Cu micropillars of around ~700 nm diameter. Although excellent material properties were obtained, the fabrication process is limited to strand-based geometries and low deposition rates. Similarly, Reiser *et al.* [21] have used electrohydrodynamic redox printing to create ~400-nm-diameter multi-metal pillars. In addition, several of these metal structures suffer from non-flat top surfaces and/or rough sidewalls, which are detrimental to the apparent mechanical properties of the structures.

There is still a lack of established additive manufacturing techniques, especially for metals, that are economical in terms of cost and speed, are scalable, and have sufficiently high resolution for micro/nano scale manufacturing. Recently, a few studies [18,21,23–25] demonstrated an in-liquid electrodeposition-based technique for additive micromanufacturing, capable of 3D printing complex metal structures without the need for post-processing. This technique typically involves delivery of a metal-containing electrolyte using a hollow microcantilever utilizing a local electroplating approach [18,21,23,26,27]. Microstructural characterization revealed that damage-free micron-size pure Cu structures could be synthesized at room temperature with template-free 3D printing, which makes it a promising technique for creating 3D nano/micro metal structures.

Most of the micron-scale 3D printing studies explored Cu microstructures for applications requiring localized fabrication, such as probe-based techniques, interconnects for electronics and high-frequency antenna coils for microwave transmission [23,28–31]. A few studies investigated structures made of platinum have already been reported in the literature [1,32], but Cu is thus far the most popular for electrodeposition due to the high Coulombic efficiency (minimum Faradaic losses because of side reactions) over a wide voltage range [23]. These structures are intended for real-life applications where they must withstand harsh loading conditions like impacts, drops, vibrations and thermal loading. However, Cu is not an ideal material from a mechanical perspec-

tive, as it suffers from a low Young's modulus, a low strength, a high strain-rate sensitivity, and thermal instability [26,33–36]. Although a few of the additive micromanufacturing techniques have made significant advances in creating complex and durable 3D structures [19], still, material property engineering for 3D printed microstructures is a largely unexplored area of research. Another limitation of additive manufacturing at a small scale is the difficulty in adapting the process for printing new materials and alloys, which often is not possible. Thus, to develop more durable solutions, core–shell structures may be adopted to enhance the strength and stability of the existing materials optimized for printing [37–39]. In this context, Ni is an attractive material as a shell for Cu micropillars due to its high Young's modulus, high strength, and good corrosion resistance. Ultrafine-grained Ni has a Young's Modulus of 200 GPa and in nanocrystalline (nc) form, its yield stress can reach values well above 1.5 GPa [40,41].

In this work, we report on the synthesis of Cu (core)-Ni (shell) structures at the micron scale with varying Ni thickness and a detailed investigation of their microstructure and mechanical properties. The dog-bone shaped Cu micropillars (core) were fabricated using the μAM technique that uses localized electrodeposition and *in-situ* detection of voxel completion in combination with a Ni coating (shell) of two different thicknesses (up to 670 nm). The microstructure and the mechanical properties of these Cu-Ni core–shell structures were explored at room temperature using a combination of dynamic *in-situ* Scanning Electron Microscope (SEM) micropillar compression experiments at strain rates ranging from 0.001 s⁻¹ to 500 s⁻¹. FE simulations model the strengthening effect of stress redistribution and geometry variation in the Cu-Ni core–shell micropillars. Post-mortem Transmission Electron Microscopy (TEM) and Transmission Kikuchi Diffraction (TKD) analysis on the deformed micropillars reveal the deformed microstructure and the related strengthening mechanisms.

2. Materials and methods

2.1. Synthesis

A schematic of the synthesis process is shown in Fig. 1. Cu microstructures were produced with a CERES μAM system (Exaddon AG, Switzerland) [23–25] (Fig. 1a and b). The substrates (area of 15 mm × 15 mm, Si / 13 nm Ti / 100 nm Cu) were sonicated for 10 min in acetone and 5 min, both in isopropanol and distilled water, before being placed in the CERES printing chamber. The reservoir of the ion tip was filled with a $CuSO_4$ solution, and the printing chamber with sulphuric acid-based solution (Printing Solution [Cu] bright, Exaddon AG, Switzerland). The printing was carried out at 24 ± 1 °C and an applied deposition potential of −0.52 V vs Ag/AgCl.

After printing, the samples were washed for 1 min in distilled water and 5 min in isopropanol, yielding pure Cu 3D structures. For the dog-bone micropillars in this study, a tip with a 300-nm-diameter aperture (Iontip, Exaddon AG, Switzerland) was used at an air pressure range of 50 mbar to 200 mbar. Each dog-bone is built up out of 104 voxels and the mean printing time of a pillar was 61 ± 1 s over the whole 10 × 10 array. The electrodeposition of the Ni coating was carried out in a three-electrode setup (Fig. 1c and d). The Cu microstructures were used as working electrodes, with an Ag/AgCl (3 M KCl) reference electrode and a soluble nickel counter electrode. The nickel sulfamate electrolyte was mixed prior to deposition, consisting of 1.13 M $Ni(SO_3NH_2)_2$ (98 %), 0.15 M $NiCl_2$ (99 %), 1 mM SDS (99 %), 5 mM $C_7H_4NNaO_3$·S·xH_2O (99.8 %) and 0.5 M H_3BO (99 %). The chemicals were used as purchased (Sigma Aldrich). The electrodes were placed in a
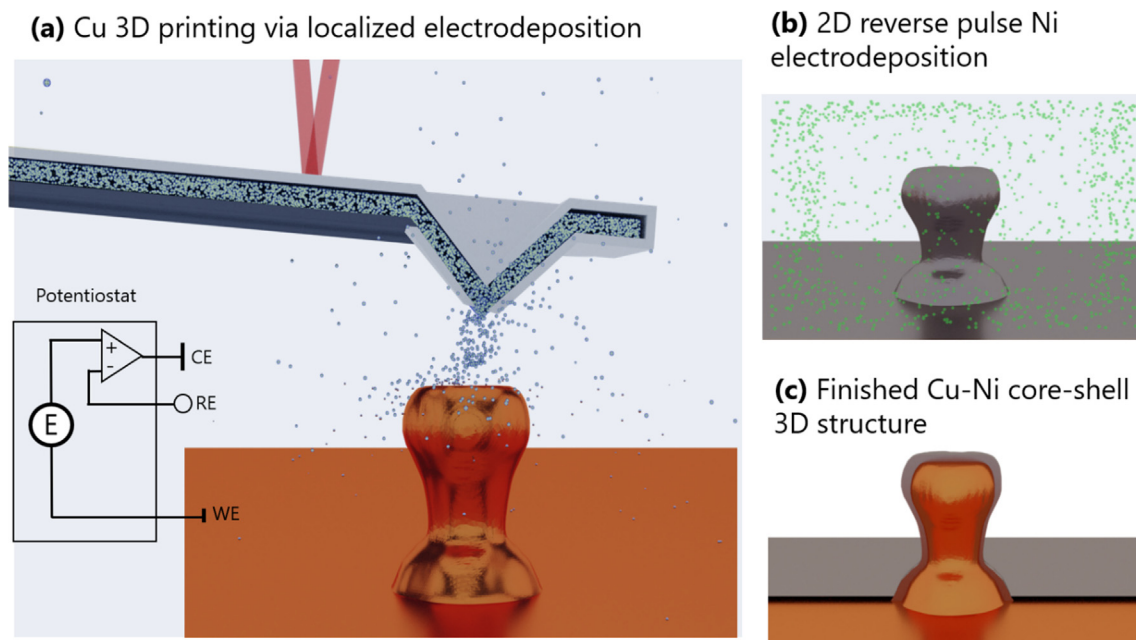
Fig. 1. (a) Cu 3D printing using a cantilever (grey) that locally supplies copper ions (blue). A potentiostat applies the deposition potential required to reduce the copper ions. Voxel completion leads to cantilever motion, which is measured by optical beam deflection (red). (b) Uniform reverse-pulse Ni electroplating (nickel ions in green). (c) Cross-section schematic showing a Cu-Ni core–shell structure. (For interpretation of the references to colour in this figure legend, the reader is referred to the web version of this article.)

double-walled glass beaker with a volume of 500 ml. The electrodeposition was carried out at 48 °C in pulsed potentiostatic mode with a deposition pulse of 50 ms at −1.2 V vs Ag/AgCl and a reverse pulse of 5 ms at 0.3 V vs Ag/AgCl. The deposition was carried out for 20 s and 62 s, respectively, for approximately 250-nm and 670-nm-thick coatings. The samples were removed from the electrochemical bath immediately upon finishing the nickel deposition process. Then they were rinsed in water, acetone, and isopropanol.

2.2. Micropillar compression at various strain rates up to 500 s^{-1}

Micro-compression tests were performed in a SEM (Philips XL30 FE-ESEM) using an *in situ* nanoindenter (Alemnis AG, Switzerland) equipped with a 20-μm-flat punch diamond tip. Strain rates ranging from 0.001 to 0.1 s^{-1} were applied using an Alemnis standard assembly nanoindenter, while strain rates ranging from 1 to 1000 s^{-1} were applied using the high-dynamic module (Alemnis AG, Switzerland). Technical details on the module can be found elsewhere [42,43]. The raw force − displacement curves were corrected by the instrument compliance and corrected for pillar sink-in into the substrate using Sneddon's correction [44]. Stresses were calculated based on the average gauge-section diameter. The intersection of a linear fit to the elastic segment of the load curve, which was offset along the strain axis by 0.2 %, marked the individual yield points. Post-mortem SEM images were recorded using a Hitachi S4800 field emission SEM (FESEM) at an acceleration voltage of 1 kV.

2.3. TKD and TEM investigation

To further investigate and analyze the material microstructure, undeformed and deformed micropillars were lifted out using SEM/FIB fabrication process. Longitudinal cross-sections along the middle were cut and thinned down to prepare the pillar samples for TKD and TEM analysis. The Scanning TEM (STEM)-High angle annular dark-field (HAADF), Energy Dispersive Spectroscopy (EDS) area maps, and Bright-field (BF)/Dark-field (DF) TEM images were acquired using a Themis 200 G3 aberration (probe) corrected TEM (Thermo Fischer) operating at 200 kV.

For all the samples, the TEM thin foils were mapped using the TKD technique to provide an overview of the orientation distribution inside the structures. All TKD patterns were collected and recorded for off-line analysis with electron beam conditions of 30 kV and 10nA, using an EDAX DigiView camera with 4x4 binning and 40-nm-step size. Furthermore, High (angular) resolution (HR) TKD cross-correlation was performed using Cross Court V.4.3 software (BLG Vantage, UK), with elastic constants of Cu (in GPa) of C11 = 168.3, C12 = 122.1, C44 = 75.7. High Resolution (HR) TKD was used to map local stresses and the geometrically necessary dislocation (GND) density distribution [45]. Indeed, the entire displacement gradient tensor, containing both strain and rotation information, can be obtained from algorithms based on determination of small shifts of features from recorded patterns using cross-correlation functions [46,47]. It is important to note that any in-plane rotation between the TEM or TKD images shown in this article is simply the result of the manual positioning of the foil in the microscopes.

2.4. Finite element simulations

Finite element simulations were performed using the commercial implicit solver Abaqus/Standard. The geometry of the printed Cu pillar was measured in 6 positions along its length and interpolated with a spline function. It was placed on a cylindrical Si substrate with a thickness of 25 μm and a radius of 25 μm to account for substrate compliance. To simulate the Ni coating, the surface of the original Cu pillar was radially translated outwards by the respective thickness of the coating. Furthermore, a cylindrical cap of Ni was added at the top of the pillar. The core–shell structure was thus modeled with two separate regions (Cu core and Ni shell) bonded by a perfect interface.

The boundaries of the substrate were fixed in all directions. The flat punch was simulated by kinematically binding all nodes at the

top of the pillar to a reference point. Isotropic elastic–plastic material behavior was chosen with a von Mises yield criterion and no strain hardening for both the Cu and Ni regions. For Cu, an elastic modulus of 137 GPa, a Poisson ratio of 0.3, and a yield stress of 0.465 GPa were used. For electrodeposited Ni, an elastic modulus of 210 GPa, a Poisson ratio of 0.3, and a yield stress of 2.5 GPa were used [41]. For Si, an elastic modulus of 127 GPa and a Poisson ratio of 0.278 were used.

The core–shell pillars and substrates were meshed with 14,500 to 16,500 quadratic hexahedral elements (16500 to 18,500 nodes) with reduced integration (C3D20R). A direct sparse solver with standard convergence criteria was utilized to solve the resulting system of equations. The pillars were compressed by 1 μm in displacement control. The reaction force was extracted and converted to engineering stress by dividing the load data by the initial smallest area of the gauge section of the pillar.

To assess the influence of a non-flat pillar top, the geometry of the top surface was estimated based on HR SEM imaging in 6 points. This profile was used to implement a non-flat pillar top in FE simulations of pure Cu pillars (see supplementary Fig. S1). In this case, the flat punch was modeled as a rigid body in hard, frictionless contact with the top of the pillar, and the pillar was compressed by controlling the downward displacement of the rigid flat punch.

2.5. Analytical modeling

An analytical expression for the elastic compliance of the micropillar was computed by integrating over the height of the pillar considering the varying cross-section that was determined using HR SEM images:

$$\frac{1}{k} = \int_0^l \frac{dz}{EA(z)} \tag{1}$$

This expression was solved for E

$$E = \int_0^l \frac{k dz}{A(z)} \tag{2}$$

Resulting in an expression allowing us to compute the unknown composite modulus based on the known unloading stiffness of the micropillar, pillar height, and variable cross-section.

Additionally, a theoretical modulus for a Cu-Ni composite based on the rule of the mixture was estimated using the following equation for isostrain condition (Voigt composite [48]):

$$E_{Cu-Ni} = \frac{E_{Ni} E_{Cu}}{E_{Ni} V_{Cu} + E_{Cu} V_{Ni}} \tag{3}$$

Here E denotes elastic modulus and V is the volume fraction. We assume that the Cu and Ni are in isostrain condition, specifically at the gauge section, where most of the deformation is supposed to be confined.

3. Results and discussion

A set of pristine Cu micropillars (dog-bone shaped) was successfully fabricated using μAM and coated with Ni of two thicknesses: 250 nm and 670 nm, which are termed as Cu-250 nm Ni and Cu-670 nm Ni, respectively. The success rate of the 3D printing of the micropillars was almost 100 %, with all the pillars having uniform microstructure. TKD and TEM were performed on the as-fabricated and deformed pillars for microstructural and chemical composition analysis (Fig. 2). TKD analysis reveals that the Cu is microcrystalline with an average grain size of 421 ± 26 nm in as-fabricated Cu-250 nm Ni, whereas Ni is nanocrystalline with an

average grain size of around 30 ± 6 nm (Fig. 2a and 2d). The microstructure is dominated by high-angle grain boundaries (>12° misorientation), mainly consisting of twin boundaries. The high-angle grain boundary (HAGB) fraction is almost 95 %, and the twin-boundary fraction was determined to be 70 % of all the HAGBs for the as-fabricated Cu-250 nm Ni sample. We expect all pillars to have the same microstructure because the same conditions were used for synthesis. We assume that an uncoated Cu sample would have a similar grain structure to a coated sample; however, the slightly larger grain size observed in the coated samples could be due to annealing effects, as the Ni was deposited at 48 °C. Fig. 2e shows the SEM image of the as-fabricated Cu-250 nm Ni pillar on a TEM grid after thinning. Further TEM/EDS investigation of as fabricated Cu-250 nm Ni sample demonstrates that a uniform layer of Ni is present (red) on the Cu micropillar (blue), particularly at the gauge section (2e). The Ni coating thickness is determined to be 250 ± 20 nm and 670 ± 30 nm for Cu-250 nm Ni and Cu-670 nm Ni samples, respectively. It is important to note that the images may not accurately represent the Cu pillar's dimensions because the pillar's cross-section lamella could be slightly away from the middle cross-section. The Ni-coating thickness, however, should not be affected. A clear interface between Cu and Ni is evident from Fig. 2d − 2e, with only a slight intermixing of Cu and Ni. It is well known that Cu and Ni can inter-diffuse and form a solid solution easily due to their similar atomic radii, the same face-centered cubic structure and similar electronegativities [49–51]. In this work, we did not observe a large degree of inter-mixing of Cu and Ni at the interface, probably due to the low deposition temperature of Ni (48 °C), which is not high enough for significant diffusion of Cu into Ni or vice versa [52]. This lack of diffusion is beneficial for the purpose of this work as it allows an enhanced study of the effect of the interface and the coating on the apparent strengthening of the pillars. The same methodology can be applied to other material systems in the future.

Uncoated and coated Cu micropillars were subjected to in-situ SEM compression at different strain rates ranging from 0.001 s⁻¹ to 500 s⁻¹. TKD analysis was performed on the deformed Cu-250 nm Ni and Cu-670 nm Ni micropillars, as shown in Fig. 2b and 2c. TKD IPF maps reveal that the deformed pillars have similar grain sizes (448 ± 30 nm and 481 ± 36 nm for deformed Cu-250 nm Ni and deformed Cu-670 nm Ni, respectively), but show a slightly higher twin-boundary fraction compared to their undeformed counterparts. For instance, the average Cu grain size for the undeformed Cu-250 nm Ni sample is determined to be 421 ± 26 nm, similar to 448 ± 30 nm for deformed Cu-250 nm Ni. However, the twin boundary fraction increased from 70 % to 80 % in the deformed Cu-250 nm Ni sample. It is evident that there is no preferential texture in the deformed and undeformed pillars (Fig. 2a–c).

The representative stress–strain curves from *in situ* micropillar compression of uncoated Cu micropillars and Cu micropillars with Ni coating of 250 nm and 670 nm at strain rate 0.001 s⁻¹ are outlined in Fig. 3. It could be shown by FE simulations of non-flat pillars that the non-linear region at the start of all three tests is caused by the uneven top surface of the pillar in contact with the flat punch (see Figure S1 in supplementary for details). In the initial stage of contact establishment, an outer ring is deformed first elastically and then plastically by the flat punch. This ring is subsequently flattened out, leading to a complete establishment of contact on the entire top surface. In this stage, the force–displacement curve shows a second linear regime representing the overall micropillar's elastic behavior. This regime is followed by a second yield point, which corresponds to the onset of plastic deformation in the gauge section. Because the initial nonlinearity in the curves is caused by a geometrical imperfection at the top of the pillar caused by the fabrication process and does not influence the stress state in the gauge section, the initial non-linear region can be
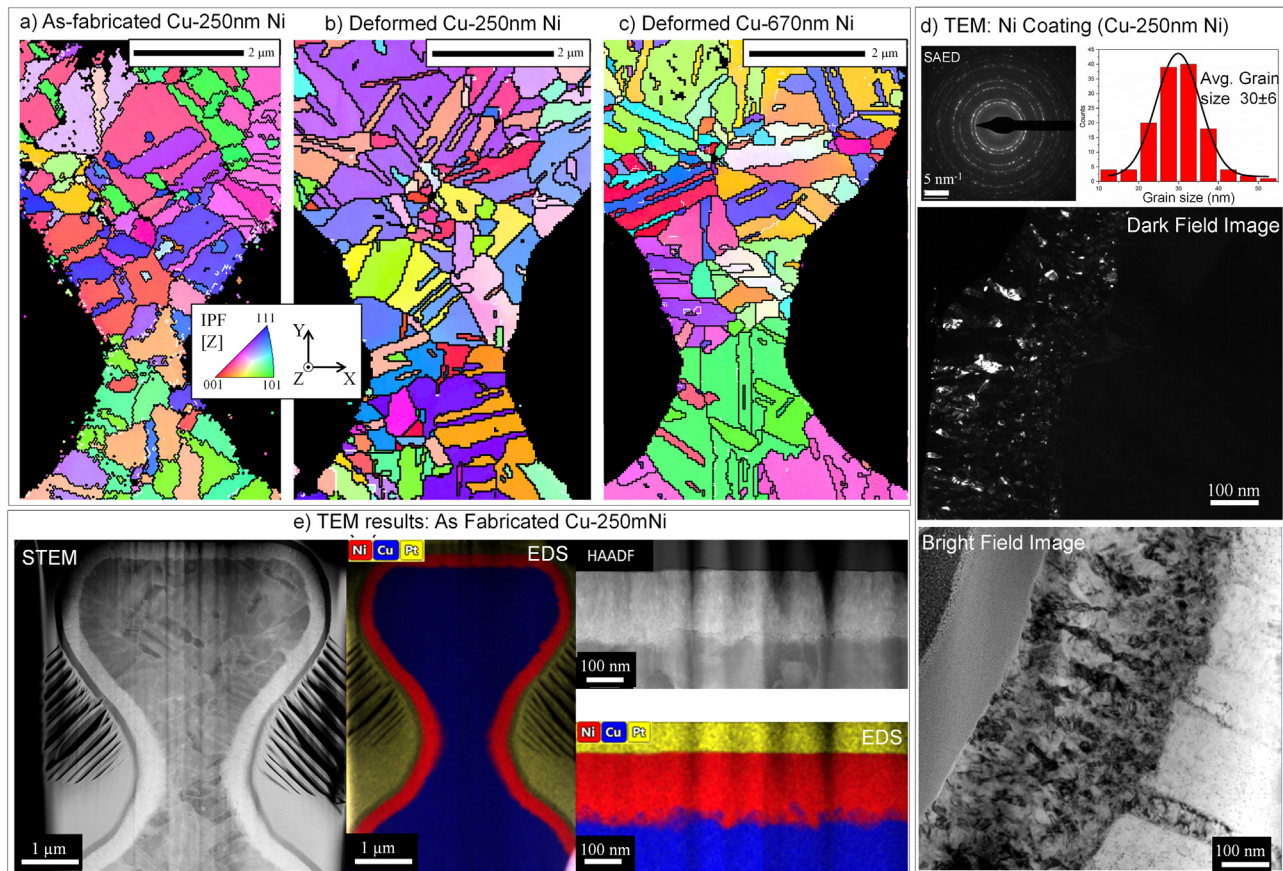
Fig. 2. TKD orientation maps obtained from the a) as-fabricated Cu-250 nm Ni micropillar, b) deformed Cu-250 nm Ni micropillar and c) deformed Cu-670 nm Ni samples, d) TEM analysis of Ni coating in as-fabricated Cu-250 nm Ni samples consisting Ni grain-size chart, dark field image, bright field image and a SAED (selected area electron diffraction) pattern e) TEM images of the as-fabricated Cu-250 nm Ni micropillar showing uniform Ni coating thickness (in red) on the Cu micropillar (in blue) using EDS and STEM mode. (For interpretation of the references to colour in this figure legend, the reader is referred to the web version of this article.)
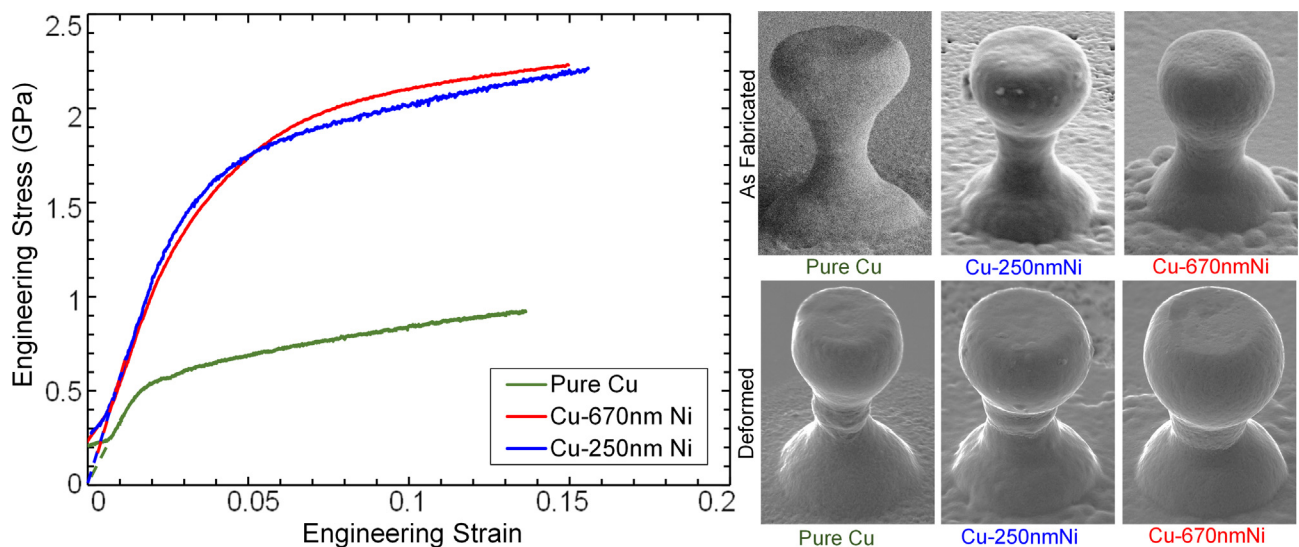

Fig. 3. Representative stress–strain curves of pure Cu, Cu-250 nm Ni and Cu-670 nm Ni are compared with SEM images (on the right) of their micropillars before and after deformation.

ignored for further analysis. It is worth noting that all tests performed on multiple pillars for each configuration showed a highly repeatable behavior. For the stress calculation, the minimum diameter at the gauge section in the middle of the pillar was used, as plastic deformation is most likely to occur in the middle due to the minimum cross-sectional area.

By considering the varying cross-section of the micropillar in an analytical model of the compliance, the elastic modulus of the Cu

deposit was determined to be around 130 GPa, which matches remarkably well with the previously reported modulus of nano-grained Cu [36,53]. The apparent moduli of Cu-250 nm Ni and Cu-670 nm Ni are 148 GPa and 150 GPa, respectively, which is again close to the values 148 GPa (volume fraction, Cu:Ni ∼ 3:1) and 160 GPa volume fraction, Cu:Ni ∼ 1:1.3) estimated using composite theory. Here we assume that the Cu and Ni are in isostrain condition at the gauge section during compression such that a Voigt average is representative of the loading situation. From the obtained modulus values, it is inferred that the composites are fully dense and contain pure Cu and Ni, which was also confirmed by TEM EDS results (Fig. 2). The 0.2 % offset yield stress of pure Cu is calculated to be 0.46 ± 0.02 GPa, which agrees well with previous studies on microcrystalline Cu with grain size ∼ 400 nm. Recently, Ramachandramoorthy *et al.* [26] studied Cu fabricated at various strain rates using the same electrodeposition-based 3D microman-ufacturing technique. They reported the yield stress to be ∼ 0.4 GPa for Cu with a grain size in the grain size range of 400 nm to 1000 nm and that yield stress was strongly dependent on the external pillar dimension-to-average internal grain size ratio (η∼1–5). In the present work, the average Cu grain size is close to ∼ 450 nm for all the pillars with η∼6–7, which suggests that the yield stress matches well with the reported value of 0.4 GPa for the grain size and η range provided [26]. The slightly increased yield stress compared to the earlier study can be attributed to a smaller average grain size and a higher η value in the present case.

More remarkably, we notice a significant strengthening (more than three times higher yield stress, 1.50 ± 0.15 GPa vs 0.46 ± 0.02 GPa) in Cu-250 nm Ni core–shell structure compared to pure Cu. Interestingly, increasing the thickness of the Ni layer from 250 nm to 670 nm exhibits little effect on the strength of the composite, which ascertains that a thin layer of Ni would be enough for the strengthening of Cu micropillars. We prpose that the deformation originates in the Cu core first, which is restricted radially by the Ni layer until the Ni layer itself starts to deform plastically, at which point plateau stress is reached. The yield strength of the nanocrystalline Ni that was deposited using similar electrolyte and deposition conditions was found to be around 2.5 GPa using *in-situ* micropillar compression [41]. This high-strength nanocrystalline Ni is responsible for the exceptional -apparent - hardening of these core–shell structures, resulting in an almost 2 GPa high flow stress at 10 % strain. This is indeed a promising material system where the pure Cu core has high elec-trical conductivity while the outer Ni layer provides the required mechanical strength and durability. Also, the shape and dimension of the 3D printed objects are retained while increasing the strength drastically.

The advantage of 3D-printed pillars resides in the pristine state of the pillars, without damage, and a smooth surface, as shown in Fig. 3b. All pillars failed at the gauge section, which validates our assumption to use the smallest diameter for stress calculation. Majorly, all Cu micropillars deformed in a similar manner, which is coherent barreling, as represented in Fig. 3b. This deformation mode has been observed in previous studies on fine-grained Cu [54]. Recently, Ramachandramoorthy *et al.* [26] reported similar deformation behavior in 3D printed ultrafine grained Cu with grain size ∼ 170 nm. Here, we note that Cu and Ni are co-deforming in the Cu-250 nm Ni and Cu-670 nm Ni composites, which is impor-tant for homogenous and gradual deformation.

These structures are intended for real-life applications where they are expected to withstand harsh loading situations like exter-nal impact and dynamic loadings such as drops or vibrations. Therefore, the structures were tested at various application-relevant strain rates. Fig. 4 shows the rate-dependent mechanical response of pure Cu and Cu-Ni core–shell structures at room tem-perature. The strain rates range from 0.001 s^{-1} to 500 s^{-1}. The
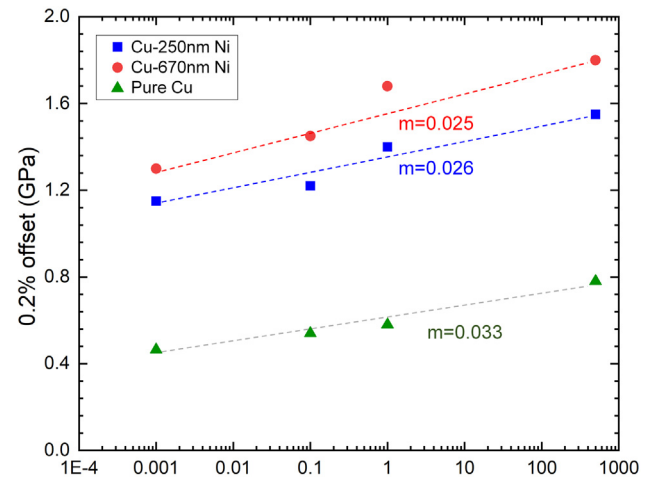

Fig. 4. Extracted 0.2 % offset yield stress values of pure Cu, Cu-250 nm Ni and Cu-670 nm Ni as a function of strain rate.

effect of adiabatic heating based on the power generated at high strain rates was ignored because it was found to be negligible (in the range of ∼ 0.01 K) for 3D-printed pure Cu micropillars using FEM simulations [18]. Both the pure Cu and the Cu-Ni structures show strong strain-rate dependency. For quantitative analysis, the strain-rate sensitivity *m* was determined using the 0.2 % offset yield stress (σ) and the different strain-rate ($\dot{\varepsilon}$)-based equation as shown below:

$$m = \frac{\partial ln\sigma}{\partial ln\dot{\varepsilon}} \qquad (4)$$

The 0.2 % offset yield stress as a function of strain rate is reported in Fig. 4. Pure Cu samples exhibit a strain rate sensitivity (*m*) of 0.033, which falls within the range of previously reported values for UFG Cu from 0.02 to 0.06 [26,55]. This validates our approach and test setup to calculate the strain-rate sensitivity. Other samples with Ni coating on top Cu-250 nm Ni and Cu-670 nm Ni show a similar but slightly lower value of *m*, i.e., 0.025 and 0.026, respectively, Cu and nanocrystalline Ni (around 0.02) [56]. Note that we did not observe any change in deformation behavior as all the pillars failed through coherent barreling.

The apparent activation volume is kinetically an effective signa-ture of the operative deformation mechanisms [57]. An estimate of the apparent activation volume can be obtained from the different strain rate experiments using the following equation [42]:

$$\Omega = \sqrt{3}k_BT\frac{\partial ln\dot{\varepsilon}}{\partial \sigma} \qquad (5)$$

where *T* is the temperature (in Kelvin) and k_B is the Boltzmann con-stant. We calculated the activation volume for pure Cu to be around 16.25 b^3, assuming the Burger vectors to be 0.255 nm for a perfect dislocation in Cu. This low activation volume, close to 10 b^3 points towards dislocation nucleation-based deformation at yield. This observation is in line with the deformation mechanism discussed in the literature [26,55]. It has been reported previously that a low stacking-fault metal, like Cu, has a preferred deformation pathway, which is usually a partial dislocation nucleation from triple points [58]. For the Cu-Ni core–shell structures, estimating the activation volume is difficult as deformation occurs simultaneously in both Cu and Ni. Most likely, Cu has already plastically deformed to a sig-nificant amount, and Ni has also started to yield at the apparent point of yielding of the composite structure. Using the dynamic test-ing, we see evidence that the Cu-Ni interface is not significantly impacting the strain-rate behavior of these composites, because

the strain sensitivity of the composite remains in the range of strain-rate sensitivity values for pure Cu and Ni.

3.1. Strengthening mechanism of Cu in Cu-Ni core–shell structure

To get more insight into the strengthening and deformation mechanisms of the Cu-Ni core–shell structures, complementary FE simulations and detailed TKD and TEM analysis on the deformed pillars were carried out. FE simulations were performed on five configurations - pure Cu, Cu-100 nm Ni, Cu-250 nm Ni, Cu-670 nm, and Cu-1000 nm Ni - using the implicit solver ABAQUS/Standard. The simulated load–displacement data is compared with the experimental data as shown in Fig. 5a. We observed a remarkable similarity between experimental and simulated load–displacement data for pure Cu, which helped us to validate the simulations. However, non-identical loading slopes for simulation and experiments (even after ignoring the initial non-linearity in the experimental data due to non-flat sample top as mentioned before) are evident in Fig. 5, even though the same elastic modulus is used for simulation as obtained from the experiments. It is common for micropillar experiments to observe a lower loading slope due to initial misalignment between the flat tip and the pillar top and due to dissipative processes such as friction and plastic flow near the contact [59]. Therefore, the elastic modulus was calculated from the unloading segment of the stress–strain curve (more details can be found in the experimental section).

In terms of yield force and maximum forces, we note an outstanding similarity between experimental and simulated load–displacement data for pure Cu, Cu-250 nm Ni, and Cu-670 nm Ni. All three samples demonstrate similar yield force values and reach similar maximum force values. In Fig. 5b, the yield force and maximum force at 0.8 % strain obtained from experiments are very well matched by the FE simulation. This validated our simulation and experimental data; thus, we extended the FE simulations to predict the mechanical response of two more configurations, Cu-100 nm Ni and Cu-1000 nm Ni. Here we observed a linear trend for the yield force and maximum force as a function of Ni coating thickness and by fitting a line (with high R^2 values > 0.97) to it, we obtained an empirical relationship between the yield force vs Ni-coating thickness and between the maximum force vs Ni-coating thickness:

$$\sigma_{yield\ force}(mN) = 0.0337(mN/nm) * \lambda(nm) + 4.5306(mN) \qquad (6)$$

$$\sigma_{max.\ force}(mN) = 0.0121(mN/nm) * \lambda(nm) + 3.2334(mN) \qquad (7)$$

where λ is the Ni coating thickness. The relationships obtained can be used to predict the mechanical properties such as yield force and maximum force of the Cu-Ni core–shell structure as a function of Ni-coating thickness and provide valuable insight into design strategies for stronger and more robust composite materials for future applications.

It is important to note that there is a sharp transition from the elastic to the plastic regime in the simulation, while the transition is more gradual in experiments. Even though yield force and max. force were very well matched by the FE simulations; strain hardening was apparently overestimated. This overestimation is attributed to the strength of the Cu-Ni core–shell structure being dictated by the stronger and stiffer nanocrystalline Ni shell through load redistribution and confinement effects. As the Ni-coating thickness increases, the composite gets stronger (simulated up to a 1000-nm-thick Ni Coating), which is expected according to the rule of mixture. Note that the FE simulation simulates the material behavior on a continuum level based on von Mises plasticity and does not explicitly consider the grain boundary or interface boundary effect or any dislocation or diffusion-based deformation mechanism. Furthermore, the differences in apparent

stiffness and strain hardening may be caused by the uneven top surface of the real micropillar, which were not accounted for in the finite element analysis. Further simulations including an uneven top surface and contact conditions between a rigid flat punch and the micropillar showed a clear influence of the ring-like surface artefact present in the real structures (Supplementary Fig. S1). In this case, the surface is plastically flattened following establishment of the contact causing the appearance of an artificial apparent yield point in the initial loading curve. As this reduces initial contact area and leads to early onset of plasticity inside the structure, this reduces the apparent stiffness of the structure and thus the precision of the strain estimation from the micropillar compression experiment.

It has been reported that interface crystallography is critical in dictating the core–shell structure's mechanical performance [60]. For example, a semi-coherent interface in a Al-Ni (fcc-fcc) core–shell structure exhibits a higher strengthening with increasing Ni-coating thickness as compared to a coherent interface Cu-Ni (fcc-fcc), which shows little effect of Ni coating thickness on strengthening [60]. In the case of a coherent interface, dislocations can move relatively easily, whereas, dislocations would be pinned/blocked at the semi-coherent or incoherent interface, resulting in strain hardening of the material. On the contrary, a gold shell has been shown to weaken a single crystal silver particle (core) by acting as a dislocation source, causing premature failure of the core material [61]. An interesting observation in the present work is that despite the presence of a Cu-Ni (fcc-fcc) interface, we observed considerable strengthening of the Cu composite with 250 nm of Ni Coating. Two different strengthening mechanisms have been observed due to the Cu-Ni interface, depending on the coherency of the interface [62–68]. In the case of a coherent Cu-Ni interface, the strengthening is due to homogenous nucleation of the dislocations at the interface and their subsequent interactions [62,63]. While in a semi-coherent interface, pre-existing misfit dislocations play a major role in strengthening [64,67,68]. In both cases, dislocations eventually propagate through the interface, but the interface acts as a strong barrier to the dislocation motion. Hence, the Cu-Ni interface must be responsible for a higher strengthening by restricting the motion of dislocations or twins, which originate either in the Cu or at the interface [69,70].

Other factors that could be important for the deformation mechanism of Cu-Ni composites are related to the Cu and Ni grain structures and their individual deformation mechanisms. As mentioned above, Cu is microcrystalline and the dislocation nucleation-based deformation mechanism is more probable at room temperature and quasistatic strain rates [26]. Conversely, Ni is nanocrystalline, with a grain size of ∼ 30 nm. Previous studies on nc Ni with a grain size of 20 to 30 nm have concluded that dislocation nucleation at the grain boundaries and at triple junctions is the dominant deformation mechanism at quasistatic strain rates [41,58,71,72]. This deformation mechanism switches to grain boundary sliding and grain rotation [73,74] for a Ni grain size below 15 nm. For microcrystalline Cu (grain size ∼ 400 nm) and nc Ni (grain size ∼ 30 nm), deformation is demonstrated to be controlled by dislocation nucleation and dislocation propagation-based mechanism at quasistatic strain rates. Moreover, the sample-size to grain-size ratio has also been observed to affect the mechanical response of nc Ni [75,76]. For instance, yield strength and deformation mechanisms were considerably different for micropillars compressed with different diameters (160 ± 30 nm and 272 ± 30 nm) but with similar Ni grain size (∼30 nm) [75]. In other words, the yield strength and deformation mechanism would change if the number of grains in a sample is less than ∼ 10 measured along the diameter. Thus, we expect to observe a different strengthening behavior between Cu with a thinner nc Ni coating (50–100 nm, corresponding to 2 to 4 grains) and Cu with a thicker
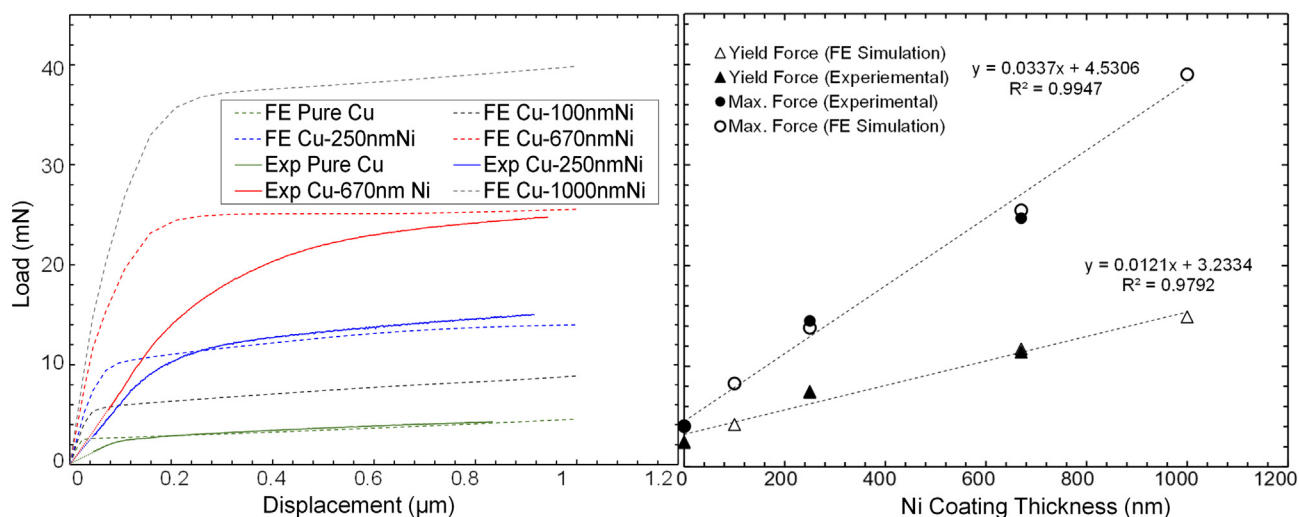
Fig. 5. (a) Comparison of load–displacement data obtained from experiments and FE simulation. The dotted lines represent data from FE simulation, and smooth lines show data obtained from experiments. (b) Yield force and maximum force extracted from the FE simulation and experimental load–displacement data are plotted as a function of Ni coating thickness. Lines were fitted and linear relationship were obtained from the FE simulation data for both yield force and maximum force with respect to the Ni coating thickness.

nc Ni coating (250 nm and above, corresponding to>10 grains) due to the possible size effect. However, FE simulation results only show a strengthening behavior according to the rule of mixture for all the coating thicknesses ranging from 100 nm to 1000 nm (Fig. 5) and the potential size effect in 100 nm coated sample could not be captured. Therefore, the microstructure needs to be considered in addition to the geometrical effects of the core–shell structure. At the same time, FE simulations helped us to validate our experimental setup and provided a valuable insight about the possible strengthening of the structures by load and strain distribution.

From experimental data in Figs. 3 and 5, we hypothesize that the dislocations and twins are initially nucleating in Cu (Cu is much weaker than Ni) at high-angle boundaries and at the Cu-Ni interface. Then their interactions with each other and the interface cause the strain hardening in the composite, whilst Ni is still elastically deforming and resisting the radial expansion of the Cu [62–67]. From a mechanics perspective, this could be interpreted by a decrement in the tangent stiffness of Cu while it is plastically deforming. However, Ni is still elastic and absorbs a significant proportion of the additional load, leading to strong apparent strain-hardening (stress redistribution). Once Ni also undergoes yielding, the hardening saturates. When stress is sufficiently high for the dislocations to cross the interface, the overall composite is yielding. In case of stress–strain data in Fig. 3, It can be argued that the yield stress of the Cu 250-nm Ni structure was already very close to the yield stress of pure nc Ni. In principle, a higher Ni thickness should lead to higher strength, but it is not the case, as shown in stress–strain curves (Fig. 3). The upper bound for strength is the strength of the Ni. Therefore, a thicker coating of the same material does not increase the yield stress, as the strength of the composite will asymptotically approach the strength limit of the coating.

To understand the potential contribution of the Cu-Ni interface and plastic strain distribution in the strengthening of the core–shell structures in detail, TKD and TEM analysis of the deformed pillars were carried out. Another remarkable similarity is observed in the position of the plastic strain region identified in FE simulations as well as experiments for the post-deformed Cu-250 nm Ni and Cu-670 nm Ni micropillars (Fig. 6). High-resolution kernel average misorientation (HR-KAM) maps obtained from the TKD

analysis of the deformed pillars of the Cu-250 nm Ni and Cu-670 nm Ni samples are shown in Fig. 6a-b. Note that KAM has been reported to be dependent on the GND density [77], i.e. lattice curvature, and to correspond to the applied macroscopic strain when averaged over multiple grains or entire measurement fields [77–79], thus often used as a qualitative measure of plastic deformation localisation The equivalent plastic strain maps of the deformed pillars obtained from FE simulations are shown in Fig. 6c -d. The majority of the deformation is accommodated in the gauge section as evident in the TKD HR–KAM map (as per legend) of the Cu-250 nm Ni (Fig. 6a), which matches well with the simulated Cu-250 nm Ni pillar after loading (Fig. 6c). The highest plastic strain is concentrated in the Ni layer indicating the importance of the outer Ni layer for strengthening. A parametric numerical study investigating the influence of coating thickness on the plastic strain and von Mises stress distributions (see Supplementary Fig. S3) showed that indeed the highest stresses appear in the Ni due to its high stiffness and yield strength. In the Cu-670 nm Ni pillar the plastically strained region is shifted upwards of the gauge section and towards the top of the pillar in both TKD HR–KAM map and simulated plastic strain map. This is possibly due to the thicker (4 µm) gauge section in the Cu-670 nm Ni structure, reducing the overall difference in the dimension of the pillar, and could cause a variation in strain distribution and stress–strain profile. This was verified again by numerical simulations varying coating thickness (Supplementary Figure S3), which showed that for thicker coatings the average stress in the Cu inside the gauge section is reduced, likely due to the stress shielding of the stiff Ni coating. The effective copper content of the composite varies with the vertical position in the specimen. Inside the gauge section, the composite strength is highest because the - significantly weaker and more compliant - copper core has a small cross sectional area compared to the stiff Ni shell leading to a redistribution of stresses in this region.

Post-mortem TEM analysis was performed on the deformed Cu-250 nm Ni and Cu-670 nm Ni pillars to get more insight into the deformation mechanism. Fig. 7(a-d) and 7(e-h) show the Cu-Ni interface of deformed Cu-250 nm Ni and Cu-670 nm Ni pillars, respectively. It is evident that Ni is nanocrystalline, in contrast to the Cu, which has bigger grains (grain-size range ∼ 400 nm). White arrows in Fig. 7a, 7c, and 7d show several dislocations pinned at
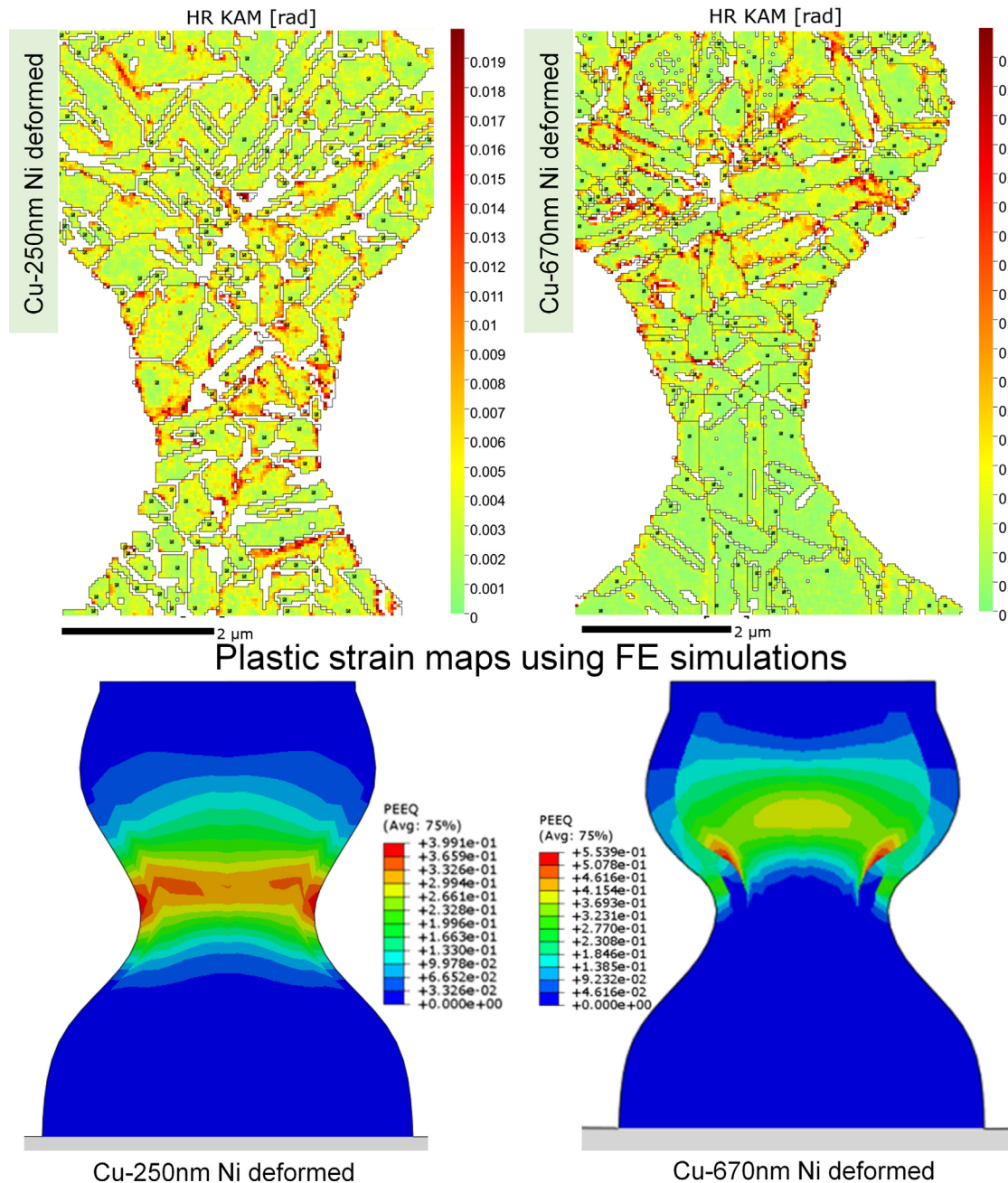
Fig. 6. (a) HR-KAM maps obtained using TKD analysis of the deformed (a) Cu-250 nm Ni and (b) Cu-670 nm Ni micropillars and equivalent plastic strain (PEEQ) maps obtained using FE simulation of (c) Cu-250 nm and (d) Cu-670 nm Ni micropillars.

the side interface (parallel to the loading direction) as well as at the top interface (perpendicular to the loading direction) in both the samples. Additionally, in Fig. 7e and 7 g) twins and stacking faults are blocked at the interface. This suggests that the interface must play a role in strengthening these composites by blocking the defects originating in Cu. This could be one of the reasons that the Cu-670 nm Ni pillar - otherwise expected to possess higher strength according to the composite theory due to the higher percentage of Ni - is not stronger than Cu-250 nm Ni. It is possible that an even thinner layer of Ni (maybe 50–100 nm) would be sufficient to provide similar strength or even higher (due to the potential size effect) in Cu-Ni core–shell structure, which would be remarkable for future composite development involving coated structures. Additionally, we have also observed dislocation cell structures in

our Cu deformed micropillars, which is consistent with the deformation characteristics observed by Zhao et al. [80] on the Cu micropillars in the micropillar size ranging from 3 μm to 5 μm.

Our results point to the presence of an optimal coating thickness for strengthening of core materials. Furthermore, interface crystallography and microstructure play an important role and must be considered while creating the core–shell structure for mechanical property improvement. FE simulation is helpful in predicting the composite's maximum strength and yield strength and could be tuned to predict the complete behavior of the composite by incorporating more information related to the microstructure of the material. The findings of this study can be extended to other material systems and can provide a pathway to enhance the mechanical properties of more complex structures, which would
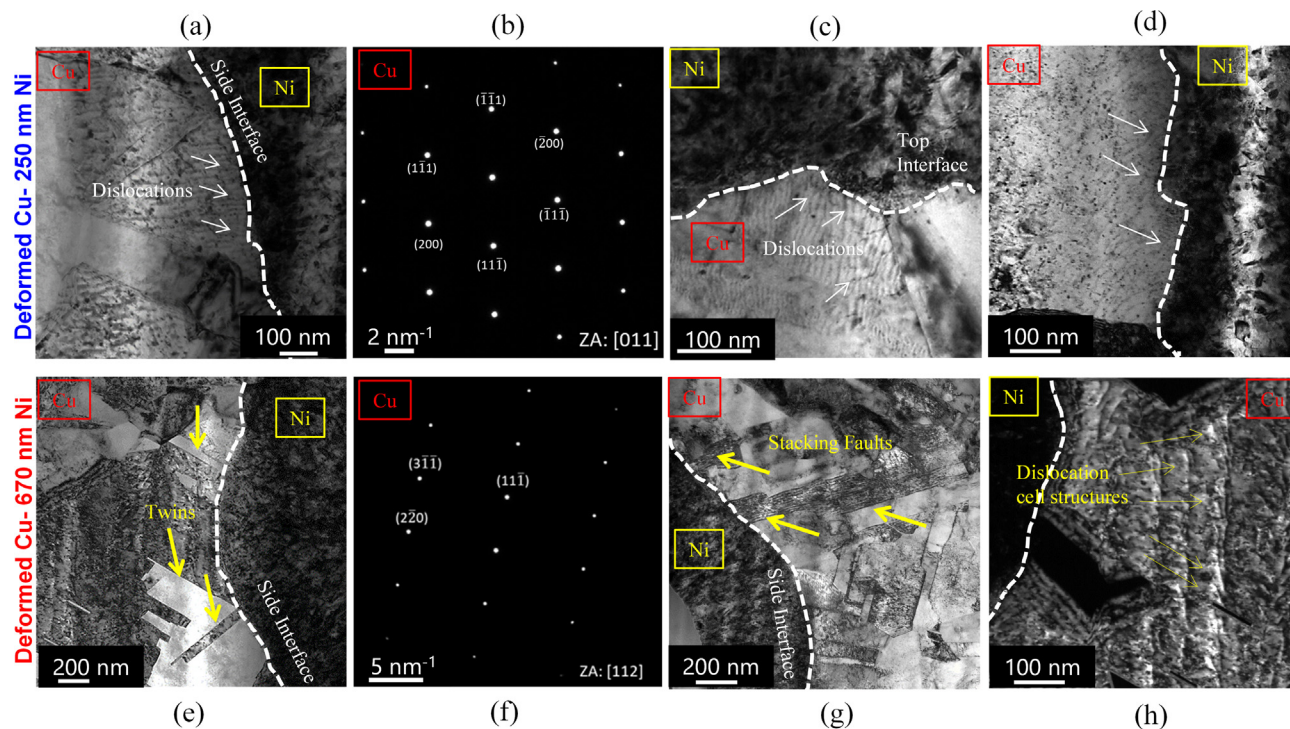
Fig. 7. HR-TEM images of the deformed micropillars of (a-d) Cu-250 nm Ni and (e-h) Cu-670 nm Ni, revealing that the dislocations, dislocation cell structures, twins, and the stacking faults are pinned at the top and the side Cu-Ni interfaces.

be critical for future structural materials at micro and nano scale. In this context, the application of our method to designing and synthesizing optimized core–shell microlattice metamaterials, whose properties go beyond those of their bulk counterparts [81–83], seems a promising pathway towards realizing strong, tough, and lightweight structural materials.

4. Conclusion

In this work, Cu-Ni core shell structure structures were synthesized by additive micromanufacturing of a Cu core using localized electrodeposition and coating with a Ni shell using global electrodeposition. These Cu-Ni core shell structures were then investigated using a combination of experiments and FE simulation to gain more insight into the effect of the Ni-coating thickness as well as the governing deformation mechanism. The following conclusions can be made:

- We observe a remarkable $\sim$ 3-fold increase in strength after coating the Cu structure with a Ni shell that is only 250 ± 20 nm thick. Interestingly, tripling the Ni shell thickness to a Cu-Ni core–shell structure with a 670 ± 30 nm-thick-Ni shell yields only a moderate increase in strength.
- Dynamic testing was performed up to 500 s^{-1}, which revealed that the strain-rate sensitive behavior of these composites is like that of the individual Cu and Ni and no apparent effect of the interfaces or of the core–shell structure on the strain-rate sensitivity is observed.
- To get more insight into the dominating strengthening mechanisms, FE simulations were performed and compared with the experimental results. The load–displacement data and plastic strain map obtained from FE simulations demonstrate clear similarities with the load–displacement data obtained from the micropillar experiment and HR-KAM map of the deformed samples using HR-TKD. From FE simulation data, we validated

our experiments and conclude that strengthening of the Cu-Ni core–shell structure is due the geometric constraints imposed by the stronger Ni layer on the Cu core and the resulting redistribution of stresses in the composite. We established an empirical relation to predict the yield force and maximum force of the Cu-Ni core–shell composite as a function of Ni-coating thickness.

- Moreover, post-mortem TEM of the deformed pillars of Cu-250 nm Ni and Cu-670 nm Ni show that the dislocations, twins and stacking faults are pinned at the Cu-Ni interface and are unable to move, until sufficient load is reached.
- Finally, it is established that in addition to the geometric confinement and stress distribution, interface crystallography and microstructure are also important factors in dictating the composite's overall mechanical response.

This study demonstrates the promise of additive manufacturing to tailor material properties via not only 3D geometry but also via material combinations to get the best out of established processes.

CRediT authorship contribution statement

Manish Jain: Conceptualization, Methodology, Validation, Formal analysis, Investigation, Writing – original draft, Visualization. **Amit Sharma:** Investigation, Visualization, Writing – review & editing. **Patrik Schürch:** Investigation, Visualization. **Nicolo Maria Della Ventura:** Investigation, Writing – review & editing. **Wabe W. Koelmans:** Investigation, Writing – review & editing, Supervision. **Xavier Maeder:** Investigation, Writing – review & editing. **Jakob Schwiedrzik:** Conceptualization, Methodology, Investigation, Visualization, Writing – review & editing, Supervision. **Johann Michler:** Investigation, Writing – review & editing, Supervision.

Data availability

Data will be made available on request.

Declaration of Competing Interest

The authors declare that they have no known competing financial interests or personal relationships that could have appeared to influence the work reported in this paper.

Acknowledgement

MJ and JS would like to thank Alemnis AG team for their valuable support during experimental setup and for providing measurement equipment.

Appendix A. Supplementary data

Supplementary data to this article can be found online at https://doi.org/10.1016/j.matdes.2023.111717.

References

[1] J. Hu, M.-F. Yu, Meniscus-Confined Three-Dimensional Electrodeposition for Direct Writing of Wire Bonds, Science 329 (5989) (2010) 313–316.

[2] L. Hirt, A. Reiser, R. Spolenak, T. Zambelli, Additive Manufacturing of Metal Structures at the Micrometer Scale, Adv. Mater. 29 (17) (2017) 1604211.

[3] B. Lenssen, Y. Bellouard, Optically transparent glass micro-actuator fabricated by femtosecond laser exposure and chemical etching, Appl. Phys. Lett. 101 (10) (2012) 103503.

[4] L.R. Meza, A.J. Zelhofer, N. Clarke, A.J. Mateos, D.M. Kochmann, J.R. Greer, Resilient 3D hierarchical architected metamaterials, Proc. Natl. Acad. Sci. 112 (37) (2015) 11502.

[5] N. Voloch-Bloch, Y. Lereah, Y. Lilach, A. Gover, A. Arie, Generation of electron Airy beams, Nature 494 (7437) (2013) 331–335.

[6] Y. Chen, Nanofabrication by electron beam lithography and its applications: A review, Microelectron. Eng. 135 (2015) 57–72.

[7] B. Wu, A. Kumar, Extreme ultraviolet lithography: A review, J. Vacuum Sci. Technol. B: Microelectron. Nanometer Struct. Process., Measure., Phenomena 25 (6) (2007) 1743–1761.

[8] F. Fang, X. Zhang, W. Gao, Y. Guo, G. Byrne, H.N. Hansen, Nanomanufacturing—perspective and applications, CIRP Ann. 66 (2) (2017) 683–705.

[9] D. Kiener, C. Motz, M. Rester, M. Jenko, G. Dehm, FIB damage of Cu and possible consequences for miniaturized mechanical tests, Mater. Sci. Eng. A 459 (1) (2007) 262–272.

[10] M.D. Uchic, P.A. Shade, D.M. Dimiduk, Plasticity of Micrometer-Scale Single Crystals in Compression, Annu. Rev. Mat. Res. 39 (1) (2009) 361–386.

[11] W. Gao, Y. Zhang, D. Ramanujan, K. Ramani, Y. Chen, C.B. Williams, C.C. Wang, Y.C. Shin, S. Zhang, P.D. Zavattieri, The status, challenges, and future of additive manufacturing in engineering, Comput. Aided Des. 69 (2015) 65–89.

[12] Y. Cai, Z. Xu, H. Wang, K.H.A. Lau, F. Ding, J. Sun, Y. Qin, X. Luo, A sequential process for manufacturing nature-inspired anisotropic superhydrophobic structures on AISI 316L stainless steel, Nanomanuf. Metrol. 2 (3) (2019) 148–159.

[13] J.G. Gigax, H. Vo, Q. McCulloch, M. Chancey, Y. Wang, S.A. Maloy, N. Li, P. Hosemann, Micropillar compression response of femtosecond laser-cut single crystal Cu and proton irradiated Cu, Scr. Mater. 170 (2019) 145–149.

[14] K.P. Karunakaran, A. Bernard, S. Suryakumar, L. Dembinski, G. Taillandier, Rapid manufacturing of metallic objects, Rapid Prototyp. J. 18 (4) (2012) 264–280.

[15] E. MacDonald, R. Wicker, Multiprocess 3D printing for increasing component functionality, Science 353 (6307) (2016) aaf2093.

[16] D. Herzog, V. Seyda, E. Wycisk, C. Emmelmann, Additive manufacturing of metals, Acta Mater. 117 (2016) 371–392.

[17] C. Körner, Additive manufacturing of metallic components by selective electron beam melting—a review, Int. Mater. Rev. 61 (5) (2016) 361–377.

[18] R. Ramachandramoorthy, S. Kalácska, G. Poras, J. Schwiedrzik, T.E.J. Edwards, X. Maeder, T. Merle, G. Ercolano, W.W. Koelmans, J. Michler, Anomalous high strain rate compressive behavior of additively manufactured copper micropillars, Appl. Mater. Today 27 (2022) 101415.

[19] S. Daryadel, A. Behroozfar, S.R. Morsali, S. Moreno, M. Baniasadi, J. Bykova, R.A. Bernal, M. Minary-Jolandan, Localized Pulsed Electrodeposition Process for Three-Dimensional Printing of Nanotwinned Metallic Nanostructures, Nano Lett. 18 (1) (2018) 208–214.

[20] Y.-L. Chen, Y. Wang, Y. Wang, B.-F. Ju, Meniscus-confined electrodeposition of metallic microstructures with in-process monitoring of surface qualities, Precis. Eng. 70 (2021) 34–43.

[21] A. Reiser, L. Koch, K.A. Dunn, T. Matsuura, F. Iwata, O. Fogel, Z. Kotler, N. Zhou, K. Charipar, A. Piqué, P. Rohner, D. Poulikakos, S. Lee, S.K. Seol, I. Utke, C. van Nisselroy, T. Zambelli, J.M. Wheeler, R. Spolenak, Metals by Micro-Scale Additive Manufacturing: Comparison of Microstructure and Mechanical Properties, Adv. Funct. Mater. 30 (28) (2020) 1910491.

[22] S. Daryadel, A. Behroozfar, M. Minary-Jolandan, A microscale additive manufacturing approach for in situ nanomechanics, Mater. Sci. Eng. A 767 (2019) 138441.

[23] L. Hirt, S. Ihle, Z. Pan, L. Dorwling-Carter, A. Reiser, J.M. Wheeler, R. Spolenak, T. Zambelli, Template-Free 3D Microprinting of Metals Using a Force-Controlled Nanopipette for Layer-by-Layer Electrodeposition, Adv. Mater. 28 (12) (2016) 2311–2315.

[24] G. Ercolano, C. van Nisselroy, T. Merle, J. Vörös, D. Momotenko, W.W. Koelmans, T. Zambelli, Additive Manufacturing of Sub-Micron to Sub-mm Metal Structures with Hollow AFM Cantilevers, Micromachines 11 (1) (2020) 6.

[25] G. Ercolano, T. Zambelli, C. van Nisselroy, D. Momotenko, J. Vörös, T. Merle, W. W. Koelmans, Multiscale Additive Manufacturing of Metal Microstructures, Adv. Eng. Mater. 22 (2) (2020) 1900961.

[26] R. Ramachandramoorthy, S. Kalácska, G. Poras, J. Schwiedrzik, T.E. Edwards, X. Maeder, T. Merle, G. Ercolano, W.W. Koelmans, J. Michler, Anomalous High Strain Rate Compressive Behavior of Additively Manufactured Copper Micropillars, arXiv preprint arXiv:2201.01582 (2022).

[27] C. van Nisselroy, C. Shen, T. Zambelli, D. Momotenko, Electrochemical 3D printing of silver and nickel microstructures with FluidFM, Addit. Manuf. 53 (2022) 102718.

[28] B.W. An, K. Kim, H. Lee, S.-Y. Kim, Y. Shim, D.-Y. Lee, J.Y. Song, J.-U. Park, High-Resolution Printing of 3D Structures Using an Electrohydrodynamic Inkjet with Multiple Functional Inks, Adv. Mater. 27 (29) (2015) 4322–4328.

[29] A.P. Suryavanshi, M.-F. Yu, Probe-based electrochemical fabrication of freestanding Cu nanowire array, Appl. Phys. Lett. 88 (8) (2006) 083103.

[30] D. Momotenko, A. Page, M. Adobes-Vidal, P.R. Unwin, Write-Read 3D Patterning with a Dual-Channel Nanopipette, ACS Nano 10 (9) (2016) 8871–8878.

[31] G. Ulisse, P. Schürch, W.W. Koelmans, V. Krozer, 3D printing of a metallic helix for traveling wave tube amplifiers operating in millimeter wave range, 2021 46th International Conference on Infrared, Millimeter and Terahertz Waves (IRMMW-THz), 2021, pp. 1-2.

[32] A.P. Suryavanshi, M.-F. Yu, Electrochemical fountain pen nanofabrication of vertically grown platinum nanowires, Nanotechnology 18 (10) (2007) 105305.

[33] A.T. Jennings, J. Li, J.R. Greer, Emergence of strain-rate sensitivity in Cu nanopillars: Transition from dislocation multiplication to dislocation nucleation, Acta Mater. 59 (14) (2011) 5627–5637.

[34] A. Wimmer, M. Smolka, W. Heinz, T. Detzel, W. Robl, C. Motz, V. Eyert, E. Wimmer, F. Jahnel, R. Treichler, G. Dehm, Temperature dependent transition of intragranular plastic to intergranular brittle failure in electrodeposited Cu micro-tensile samples, Mater. Sci. Eng. A 618 (2014) 398–405.

[35] J.S. Kim, H. Huh, Evaluation of the Material Properties of an OFHC Copper Film at High Strain Rates Using a Micro-Testing Machine, Exp. Mech. 51 (6) (2011) 845–855.

[36] R.Z. Valiev, E.V. Kozlov, Y.F. Ivanov, J. Lian, A.A. Nazarov, B. Baudelet, Deformation behaviour of ultra-fine-grained copper, Acta Metall. Mater. 42 (7) (1994) 2467–2475.

[37] L. Silvestroni, S. Failla, V. Vinokurov, I. Neshpor, O. Grigoriev, Core-shell structure: An effective feature for strengthening ZrB2 ceramics, Scr. Mater. 160 (2019) 1–4.

[38] G. Li, S. Lyu, R. Zheng, Q. Li, K. Ameyama, W. Xiao, C. Ma, Strengthening 2024Al alloy by novel core-shell structured Ti/B4C composite particles, Mater. Sci. Eng. A 755 (2019) 231–234.

[39] R.C. Longo, C. Liang, F. Kong, K. Cho, Core-Shell Nanocomposites for Improving the Structural Stability of Li-Rich Layered Oxide Cathode Materials for Li-Ion Batteries, ACS Appl. Mater. Interfaces 10 (22) (2018) 19226–19234.

[40] M. Schlesinger, Electroless Deposition of Nickel, Modern Electroplating (2010) 447–458.

[41] J. Schwiedrzik, R. Ramachandramoorthy, T.E.J. Edwards, P. Schürch, D. Casari, M.J. Duarte, G. Mohanty, G. Dehm, X. Maeder, L. Philippe, J.-M. Breguet, J. Michler, Dynamic cryo-mechanical properties of additively manufactured nanocrystalline nickel 3D microarchitectures, Mater. Des. 110836 (2022).

[42] R. Ramachandramoorthy, J. Schwiedrzik, L. Petho, C. Guerra-Nuñez, D. Frey, J.-M. Breguet, J. Michler, Dynamic Plasticity and Failure of Microscale Glass: Rate-Dependent Ductile–Brittle–Ductile Transition, Nano Lett. 19 (4) (2019) 2350–2359.

[43] R. Ramachandramoorthy, F. Yang, D. Casari, M. Stolpe, M. Jain, J. Schwiedrzik, J. Michler, J.J. Kruzic, J.P. Best, High strain rate in situ micropillar compression of a Zr-based metallic glass, J. Mater. Res. 36 (11) (2021) 2325–2336.

[44] I.N. Sneddon, The relation between load and penetration in the axisymmetric Boussinesq problem for a punch of arbitrary profile, Int. J. Eng. Sci. 3 (1) (1965) 47–57.

[45] T.J. Ruggles, D.T. Fullwood, Estimations of bulk geometrically necessary dislocation density using high resolution EBSD, Ultramicroscopy 133 (2013) 8–15.

[46] A.J. Wilkinson, G. Meaden, D.J. Dingley, High resolution mapping of strains and rotations using electron backscatter diffraction, Mater. Sci. Technol. 22 (11) (2006) 1271–1278.

[47] A.J. Wilkinson, G. Meaden, D.J. Dingley, High-resolution elastic strain measurement from electron backscatter diffraction patterns: New levels of sensitivity, Ultramicroscopy 106 (4) (2006) 307–313.

[48] W. Voigt, Ueber die Beziehung zwischen den beiden Elasticitätsconstanten isotroper Körper, Ann. Phys. 274 (12) (1889) 573–587.

[49] W.G. Nöhring, W. Curtin, Cross-slip of long dislocations in FCC solid solutions, Acta Mater. 158 (2018) 95–117.

[50] B. Onat, S. Durukanoğlu, An optimized interatomic potential for Cu–Ni alloys with the embedded-atom method, J. Phys. Condens. Matter 26 (3) (2013) 035404.

[51] J.R. Davis, Copper and copper alloys, ASM Int. (2001).

[52] B.C. Johnson, C.L. Bauer, A.G. Jordan, Mechanisms of interdiffusion in copper/nickel thin-film couples, J. Appl. Phys. 59 (4) (1986) 1147–1155.

[53] P.G. Sanders, J.A. Eastman, J.R. Weertman, Elastic and tensile behavior of nanocrystalline copper and palladium, Acta Mater. 45 (10) (1997) 4019–4025.

[54] J.Y. Zhang, J.C. Cui, G. Liu, J. Sun, Deformation crossover in nanocrystalline Zr micropillars: The strongest external size, Scr. Mater. 68 (8) (2013) 639–642.

[55] J. Chen, L. Lu, K. Lu, Hardness and strain rate sensitivity of nanocrystalline Cu, Scr. Mater. 54 (11) (2006) 1913–1918.

[56] G. Mohanty, J.M. Wheeler, R. Raghavan, J. Wehrs, M. Hasegawa, S. Mischler, L. Philippe, J. Michler, Elevated temperature, strain rate jump microcompression of nanocrystalline nickel, Phil. Mag. 95 (16–18) (2015) 1878–1895.

[57] A.S. Krausz, A deformation kinetics analysis of the stress sensitivity, Mater. Sci. Eng. 26 (1) (1976) 65–71.

[58] R.J. Asaro, S. Suresh, Mechanistic models for the activation volume and rate sensitivity in metals with nanocrystalline grains and nano-scale twins, Acta Mater. 53 (12) (2005) 3369–3382.

[59] S. Pathak, N. Velisavljevic, J.K. Baldwin, M. Jain, S. Zheng, N.A. Mara, I.J. Beyerlein, Strong, Ductile, and Thermally Stable bcc-Mg Nanolaminates, Sci. Rep. 7 (1) (2017) 8264.

[60] H. Ke, I. Mastorakos, Deformation behavior of core–shell nanowire structures with coherent and semi-coherent interfaces, J. Mater. Res. 34 (7) (2019) 1093–1102.

[61] A. Sharma, J. Amodeo, N. Gazit, Y. Qi, O. Thomas, E. Rabkin, When More Is Less: Plastic Weakening of Single Crystalline Ag Nanoparticles by the Polycrystalline Au Shell, ACS Nano 15 (9) (2021) 14061–14070.

[62] S. Shao, S.N. Medyanik, Dislocation–interface interaction in nanoscale fcc metallic bilayers, Mech. Res. Commun. 37 (3) (2010) 315–319.

[63] S.N. Medyanik, S. Shao, Strengthening effects of coherent interfaces in nanoscale metallic bilayers, Comput. Mater. Sci 45 (4) (2009) 1129–1133.

[64] S.I. Rao, P.M. Hazzledine, Atomistic simulations of dislocation–interface interactions in the Cu-Ni multilayer system, Philos. Mag. A 80 (9) (2000) 2011–2040.

[65] Z. Zhang, S. Cancan, W. Shuncheng, Luo Xing, Zheng Kaihong, Urbassek Herbert, Interaction of Dislocations and Interfaces in Crystalline Heterostructures A. Review of Atomistic Studies, Crystals (2019).

[66] I.J. Beyerlein, J. Wang, K. Kang, S.J. Zheng, N.A. Mara, Twinnability of bimetal interfaces in nanostructured composites, Mater. Res. Lett. 1 (2) (2013) 89–95.

[67] R.G. Hoagland, T.E. Mitchell, J.P. Hirth, H. Kung, On the strengthening effects of interfaces in multilayer fcc metallic composites, Philos. Mag. A 82 (4) (2002) 643–664.

[68] D. Saraev, R.E. Miller, Atomic-scale simulations of nanoindentation-induced plasticity in copper crystals with nanometer-sized nickel coatings, Acta Mater. 54 (1) (2006) 33–45.

[69] J.Y. Zhang, P. Zhang, X. Zhang, R.H. Wang, G. Liu, G.J. Zhang, J. Sun, Mechanical properties of fcc/fcc Cu/Nb nanostructured multilayers, Mater. Sci. Eng. A 545 (2012) 118–122.

[70] S. Lehoczky, Strength enhancement in thin-layered Al-Cu laminates, J. Appl. Phys. 49 (11) (1978) 5479–5485.

[71] K.S. Kumar, S. Suresh, M.F. Chisholm, J.A. Horton, P. Wang, Deformation of electrodeposited nanocrystalline nickel, Acta Mater. 51 (2) (2003) 387–405.

[72] K.S. Kumar, H. Van Swygenhoven, S. Suresh, Mechanical behavior of nanocrystalline metals and alloys, the Golden Jubilee Issue—Selected topics in Materials Science and Engineering: Past, Present and Future, edited by S. Suresh, Acta Mater. 51 (19) (2003) 5743–5774.

[73] Z. Shan, E.A. Stach, J.M.K. Wiezorek, J.A. Knapp, D.M. Follstaedt, S.X. Mao, Grain Boundary-Mediated Plasticity in Nanocrystalline Nickel, Science 305 (5684) (2004) 654–657.

[74] B. Chen, K. Lutker, J. Lei, J. Yan, S. Yang, H.-K. Mao, Detecting grain rotation at the nanoscale, Proc. Natl. Acad. Sci. 111 (9) (2014) 3350–3353.

[75] A. Rinaldi, P. Peralta, C. Friesen, K. Sieradzki, Sample-size effects in the yield behavior of nanocrystalline nickel, Acta Mater. 56 (3) (2008) 511–517.

[76] F. Dalla Torre, H. Van Swygenhoven, M. Victoria, Nanocrystalline electrodeposited Ni: microstructure and tensile properties, Acta Mater. 50 (15) (2002) 3957–3970.

[77] S.-S. Rui, L.-S. Niu, H.-J. Shi, S. Wei, C.C. Tasan, Diffraction-based misorientation mapping: A continuum mechanics description, J. Mech. Phys. Solids 133 (2019) 103709.

[78] M. Kamaya, Assessment of local deformation using EBSD: Quantification of accuracy of measurement and definition of local gradient, Ultramicroscopy 111 (8) (2011) 1189–1199.

[79] M. Kamaya, A.J. Wilkinson, J.M. Titchmarsh, Quantification of plastic strain of stainless steel and nickel alloy by electron backscatter diffraction, Acta Mater. 54 (2) (2006) 539–548.

[80] X.X. Zhao, J. Wu, Y.L. Chiu, I.P. Jones, R. Gu, A.H.W. Ngan, Critical dimension for the dislocation structure in deformed copper micropillars, Scr. Mater. 163 (2019) 137–141.

[81] H.M. Sheikh, T. Meier, B. Blankenship, Z. Vangelatos, N. Zhao, P.S. Marcus, C.P. Grigoropoulos, Systematic design of Cauchy symmetric structures through Bayesian optimization, Int. J. Mech. Sci. 236 (2022) 107741.

[82] Z. Vangelatos, G.X. Gu, C.P. Grigoropoulos, Architected metamaterials with tailored 3D buckling mechanisms at the microscale, Extreme Mech. Lett. 33 (2019) 100580.

[83] Z. Vangelatos, L. Wang, C.P. Grigoropoulos, Laser pyrolysis for controlled morphing and chemical modification on 3D microlattices, J. Micromech. Microeng. 30 (5) (2020) 055008.